Potentialities and limitations of an electro-optic probe for electric field diagnostics of cold atmospheric pressure plasma jets

Farah Aljammal, Gwenaël Gaborit, Sylvain Iséni, Maxime Bernier, Guillaume Chevrier-Gros, Lionel Duvillaret

Eur. Phys. J. D (2023)77:199
https://doi.org/10.1140/epjd/s10053-023-00781-8

THE EUROPEAN PHYSICAL JOURNAL D

Regular Article – Plasma Physics

Potentialities and limitations of an electro-optic probe for electric field diagnostics of cold atmospheric pressure plasma jets

Farah Aljammal[1,a], Gwenaël Gaborit[2,3,b], Sylvain ISÉNI[4], Maxime Bernier[2], Guillaume Chevrier-Gros[3], and Lionel Duvillaret[3]

[1] LSPM laboratory, UPR3407, Université de Sorbonne Paris Nord, 93430 Villetaneuse, France
[2] IMEP-LAHC laboratory, UMR5130, Université Savoie-Mont-Blanc, 73376 Le Bourget-du-Lac cedex, France
[3] KAPTEOS, bât. Cleanspace, 354 voie Magellan, 73800 Sainte-Hélène-du-Lac, France
[4] GREMI, UMR7344 CNRS, Université d'Orléans, 45067 Orléans Cedex 2, France

Received 24 June 2023 / Accepted 4 November 2023

Abstract. This paper focuses on the use of an electro-optic (EO) probe for the spatially and temporally resolved characterization of the electric field (E-field) associated with guided ionization waves—or guided streamers—propagating at atmospheric pressure. An AC high-voltage power supply (6 kV at 18 kHz) is used to generate guided ionization waves in helium with a cold atmospheric pressure plasma jet device (APPJ). The capabilities of this electro-optic technique are investigated with and without the discharge. This innovative technology will use to carry out the optical polarimetric analysis of the APPJ with simultaneous real-time measurement of longitudinal and radial components of the electric field vector. Last but not least, an application-based case study of the ionization waves propagating and interacting with the EO probe—being a solid dielectric target—is also reported. The results will bring realistic information on the potential perturbation induced by the EO probe itself on the E-field characterization at the macroscopic scale.

Published online: 17 November 2023

Introduction

Non-thermal atmospheric pressure plasmas consist in non-equilibrium discharges involved in active topical fields of research due to their versatility and unique potential to locally produce highly reactive radiations and chemical compounds [1]. This rich non-equilibrium chemistry results from complex coupling between the elementary processes of energy transfer through the electric field, electron dynamics, V-UV radiations and heavy charged particles (atomic and molecular ions). Their unique properties offer new perspectives and serious alternative in the field of biomedical applications (decontamination, sterilization, medicine...) [2–8], plasma-activated liquids [9–11], agriculture [12–16], active flow control [17–19] as well as industrial and catalysis processes [20–24]. Thus, the cold atmospheric pressure plasma jet (APPJ) device being part of the non-thermal plasmas (NTP) sources has drawn a significant attention. Various jet device configurations and electrical or gas supplies yield different plasma jet operations [25–27] such as ring–ring dielectric barrier discharge (DBD) [28], DBD with single-ring electrode [29], coaxial [30] and pin-to-plane [31,32]. The electrical excitation is also of significant interest involving different driving voltage waveforms such as sine (10 kHz to 200 kHz) [28,29,33,34], radio frequency (RF) [33], repetitively pulsed [32,35,36], DC [37] and self-pulsing DC [31]. The APPJs devices are usually based on DBD geometries having a capacitive electric behavior and are able to operate with various atomic or molecular gases. The ignition and the device operation are often more convenient in noble gases such as helium or argon mainly due to the higher ionization rate than molecular gases and the reduction in energy loss by electron attachment and vibrational excitations [26,38–41]. The operating gas flows into a dielectric tube, while the pair of electrodes is often powered by AC or pulsed high-voltage generator.

At atmospheric pressure, these APPJs generate guided ionization waves [27,42] which propagate over a few centimeters in a free atmosphere. After exiting the glass tube, the ionization wave is guided by the feed gas flow pattern which can be either laminar or turbulent and the in-diffusing air molecule into the noble gas [43,44]. This yields a so-called plasma plume. This active part of the discharge can be used for direct treatment regardless of the size of the objects to be treated, in particular for biological purposes and clinical field.

[a] e-mail: farahh.al.jammal@outlook.com
[b] e-mail: gwenael.gaborit@kapteos.com (corresponding author)

This is a key aspect, especially with regard to the safety requirement to the human body [45–47]. One of the prerequisites for biomedical applications, based on the direct interaction of plasma with living tissues or cells [48,49], is the diagnosis of the E-field delivered by the guided ionization waves to the biological target. Lately, in situ investigation of organic samples exposed to E-field from guided ionization waves has been reported for the first time [50] showing the direct interaction between—partially—ionized gas and living material. To some extends, it is also possible to infer from the E-field measurements, the density of charges deposited during plasma exposure [51]. Therefore, knowledge of the main plasma parameters, i.e., the E-field and the electron and ion properties are of utmost importance for the understanding and the control of plasma processes. Another major challenge is to electrically characterize the APPJ device with respect to applied voltage and the excitation frequency to understand the dynamic behavior of discharge [52–55]. Generally, an APPJ device could be divided into three parts: (1) the inter-electrode gap discharge—where the ignition of the ionization wave occurs with dielectric barrier discharge geometries; (2) the discharge in the dielectric tube—corresponding to the propagation of the guided ionization wave; and (3) the guided ionization wave expanding into the free space forming the jet plume [40,49]. E-field measurements in this type of discharge are infrequent due to the associated experimental difficulties. Nevertheless, the magnitude of the E-field is of paramount importance for experimental and theoretical work on plasma jets and their applications. It has been shown that the E-field may be responsible for various effects observed in experiments on biological samples. In plasma physics, in low ionization transient discharges, such as plasma jets, the E-field is the driver of the discharge and its amplitude is the central component which determines its behavior and the electron dynamics. For instance, the E-field is directly related to the electron energy distribution function, which subsequently governs the non-equilibrium reactive plasma chemistry [56,57]. In addition, the E-field profile is of crucial importance for the inception of streamer-based discharge. Indeed, in the general case of breakdown in non-uniform E-field, the ionization wave formation is given by the equality of the ionization integral to some threshold value (usually around 20 [58]). It is therefore very important to get more information about the E-field properties for the plasma community, whatever the experimental conditions and the measurement medium.

The focus of this work is on the spatially and temporally resolved measurements of the E-field associated with a guided ionization wave- driven plasma operating at ground pressure conditions. The discharge ignites within a long insulating quartz tube before to expand in the open space and will be characterized by means of an electro-optical method. The EO transducer provides a detailed characterization of the E-field vectorial profile behavior induced by the high voltage source that initiates the ionization process, on the one hand, and by the plasma itself, on the other hand. The interest in the characterization of E-field in plasma jet sources has been significantly growing lately [59–64] due to the potential role of E-field in biological mechanisms [65] and the impact of the action E-fields on cells [50,66,67].

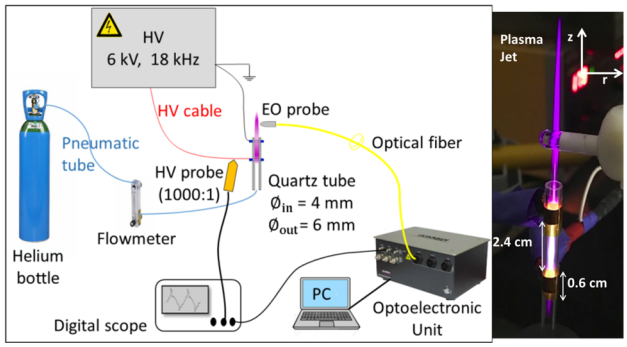

Fig. 1 Schematic of the experimental setup: on the left side, the whole experiment setup. On the right side, a photograph of the APPJ configuration, with the EO probe used to measure simultaneously two orthogonal component of the E-field vector

This paper is structured in three sections: Section 1 describes the experimental setup, including the EO measurement bench and the APPJ device. This section also reports on the calibration of the EO probe, required for the absolute measurement of the E-field vector components. Then, Sect. 2 is dedicated to the real-time and vectorial analysis of the E-field associated with the APPJ. The ionization wave propagation and the optical polarimetric pattern are also analyzed and discussed. Finally, Sect. 3 provides additional results related to the potential disturbance induced by the probe itself on the measurement of the E-field temporal and spatial profile.

1 Experimental setup

The experimental setup is shown in Fig. 1. The cold helium APPJ is generated in a dielectric barrier discharge (DBD) configuration [68].

As shown on the left side of Fig. 1, a gas bottle, delivering helium gas (Alphagaz 1, Air Liquide) is connected to a flow meter. The flow rate of $Q_v = 2$L/min is set to feed a quartz tube of 4.0 mm diameter. The velocity of the helium gas through the tube v is estimated from the flow rate, $v = \frac{Q_v}{S} = 2.6$m/s, with S the cross section of the tube. The quartz tube is equipped with two copper ring electrodes of 0.6 mm and separated with a gap of 24 mm. The grounded electrode of 35 µm thick is wrapped around the outer tube surface. The powered electrode is supplied by sinusoidal high voltage (amplitude of 6 kV at a fixed frequency of 18 kHz). The present geometry and parameters yield a mean gas flow velocity in the order of 2.6m/s within the tube and at its outlet. A laminar flow pattern is thus formed where the ionization waves will propagate.

For the electrical investigation, a high-voltage probe (TESTEC TT-HVP 15HF) was connected to the bottom wrapped electrode. The attenuation ratio of the voltage probe is 1000:1. The E-field measurements are carried out with an electro-optic sensor (eoProbe) commercialized by KAPTEOS company (more specific details in [69–71]). The probes are separated by a 5.0-m-long polarization-maintaining (PM) fiber from the KAPTEOS eoSense converter. This optoelectronic unit delivers an analog voltage proportional to the E-field component over a bandwidth spreading from 30 Hz to 30 MHz. The temporal waveforms of the voltage and the field are simultaneously recorded with a fast digital oscilloscope featuring an instantaneous bandwidth of 70 MHz (sampling rate of 1 GS/s). All the acquired waveforms are triggered using the voltage signal. In order to perform an absolute measurement of the E-field magnitude, the EO setup requires being absolutely calibrated. For that purpose, the probe is placed in between two parallel electrodes, separated by 40 mm and polarized with a voltage generator producing a synthesized AC waveform at fixed frequencies. This is to properly generate a homogeneous field vector in magnitude and orientation. The standard deviation of the field strength distribution in the probe location has been measured and is weaker than 0.2 dB. The frequency bandwidth of this field generator reaches more than 20 MHz.

The theoretical and experimental responses of the system with respect to the field magnitude are given in Fig. 2.

The linearity curve is obtained by varying the magnitude of the E-field, either using a frequency synthesizer in the frequency domain (blue signals on Fig. 2) or using the high voltage source in the time domain (red signals on Fig. 2). The output signal of the EO setup is measured either with a spectrum analyzer or with the digital scope. The EO response with respect to the field strength exhibits a dynamics greater than 120 dB (limited to about 80 dB in the time domain due to the increase in the noise). A very good agreement is observed between experimental data and expected fitting curve. Moreover, even if further measurements will all be performed in the time domain for quite high field strength, the measurement in the frequency domain allows extracting a minimum detectable field much lower than 1.0 V/m. Finally, this experimental result permits determining experimentally the scaling factor between the output signal of the setup and the actual field strength. This factor is called antenna factor AF for a RX antenna is calculated as the ratio $AF = \frac{|E_i|}{V_{\text{out}}}$, with $|E_i|$ the modulus of the measured field component and V_{out} the output useful signal. The numerical value of the antenna factor is here $AF = 1.65$ (kV/m)/mV or 124 dB/m in the logarithmic scale. The equation used to fit the link between the E-field and the output signal P_{EO} reads,

$$P_{EO} = 10 \log_{10} \sqrt{P_{\text{Noise}}^2 + P_{\text{Mod}}^2}, \quad (1)$$

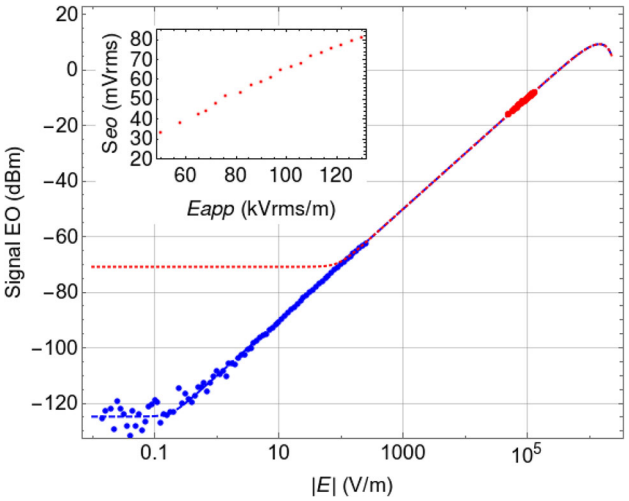

Fig. 2 Theoretical and experimental responses of the EO probe used, as a function of the E-field magnitude. The blue dashed curve is the fitting curve corresponding to a characterization in the frequency domain, with a noise floor obtained in a resolution bandwidth of 3.0 Hz. Blue dots correspond to the experimental data. The red dotted curve is the fitting curve corresponding to a characterization in the time domain, with the lowest noise of the oscilloscope (measured with an averaging of 64 samples). Red dots are associated with the experimental data. The inset represents the raw EO signal as a function of the applied voltage in the time domain using the high voltage source

with P_{Mod}, the electrical power directly associated with the electro-optic modulation and optoelectronic conversion, and P_{Noise}, the noise level of the system measured either on the spectrum analyzer or on the oscilloscope. The form of the equation explains the curvature of the fitting curves in the vicinity of the noise floor (bottom of the curves). P_{Mod} can be written as a function of R, the resistive load of the photodiode, η its responsivity and the actual modulation of the optical power P_{modopt}:

$$P_{\text{Mod}} = R \times (\eta P_{\text{modopt}})^2 . \quad (2)$$

The whole optical response, giving P_{modopt}, is expressed as follows:

$$P_{\text{modopt}} = P_{\text{optmean}} \left(0.5 - \cos^2 \left(\alpha E + \frac{\pi}{4}\right)\right), \quad (3)$$

with P_{optmean} the mean optical power, and α the linear coefficient between the E-field to be measured E and the optical modulation P_{modopt}. This later coefficient α is linear with the length of the crystal and with its involved electro-optic coefficients. The form of P_{modopt} includes a cosine function illustrating the saturation of the signal for intense field strength (see top of curves in Fig. 2).

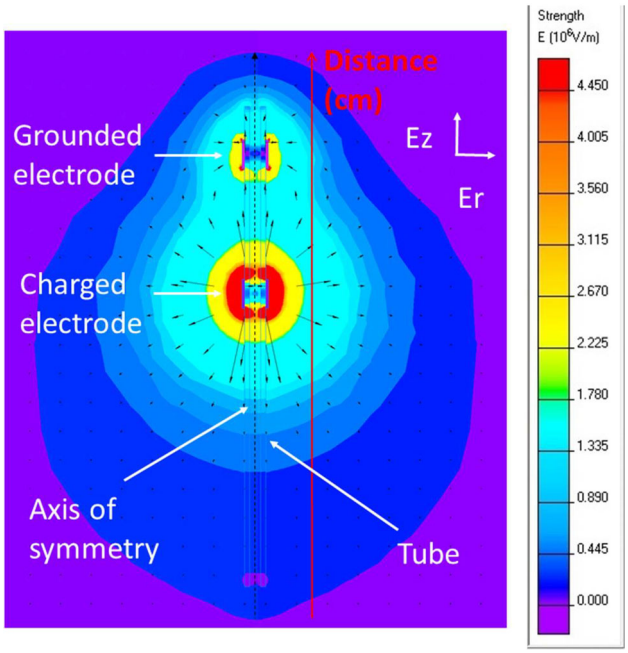

Fig. 3 Computed spatial distribution of the E-field with the structure under test at 6 kV (FEM simulation). The spatial distribution is then analyzed along the vertical red line

2 Experimental results and discussions

For all the experimental results presented in this paper, the operating gas was helium, and the applied peak voltage and pulse frequency were $V = 6$kV peak-to-peak at $f = 8$kHz, respectively.

2.1 Spatial distribution of the Laplacian field along the tube and Electrostatic simulation

The goal of the measurement campaign is to give an exhaustive spatiotemporal characterization of the E-field and this experimental study begins with the analysis of the field distribution in the vicinity of the tube along the *Z-axis*. The measurements are performed with gas flow off. The results are presented in Figs. 3 and in 4, for numerical simulations and for the comparison with the measured data, respectively.

Using finite element method (FEM), a 2D numerical simulation has been performed to provide a preliminary analysis of the spatial distribution of the field induced by the electrodes configuration set with an AC voltage potential. The geometry is meshed with more than 200 000 nodes. The relative permittivity $\epsilon_r = \epsilon/\epsilon_0$ for all elements are considered like quartz and air. Under the conditions corresponding to the experimental parameters, the model predicts the appearance of the Laplacian field with the order of several hundred of kV/m in the vicinity of the charged electrode. The comparison between the simulations and the experimental data is presented in Fig. 4.

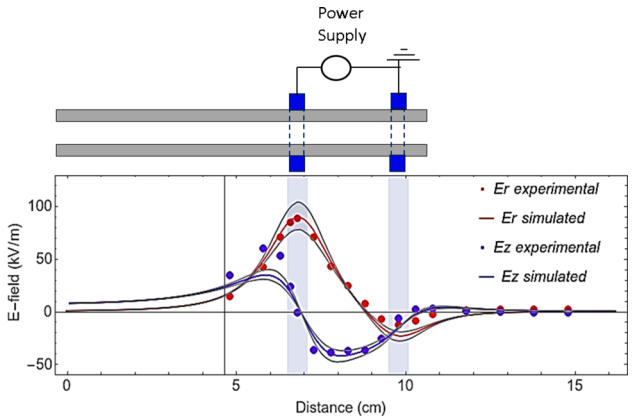

Fig. 4 Spatial distribution of E_r and E_z in the vicinity of the tube. The position of the electrodes are indicated in light blue. Red dots and the corresponding curve are the measured and simulated value of E_r, respectively. Blue dots and related curve correspond to the measured and simulated value of E_z, respectively. Surrounding black line give the uncertainty to eventual error in the probe positioning (maximum 1.0 mm for the distance between the probe and the tube)

In order to analyze this distribution, let us follow for example the radial component (red curve). The graphic is divided into three parts. From 0 cm to 6.5 cm (zone just before the charged electrode), the field increases linearly and gradually to reach its maximum greater than 80 kV/m in the vicinity of the charged electrode. After this electrode, the field decreases linearly between the two electrodes to reach another local negative maximum in the vicinity of the grounded electrode. Then, it vanishes and remains approximately equal to zero beyond (in between the grounded electrode and the rest of the setup). A significant agreement between the experiment and the simulation for field distribution is observed. Concerning the component E_z, it should be rigorously zero in the vicinity of the charged electrode, what is observed both on simulation and experiment. As expected, E_z reaches its maximum value in between the electrodes.

2.2 Electric field vector measurements: mapping of radial and longitudinal E-field components associated with the APPJ

The radial component E_r of the E-field vector is here firstly recorded by the transverse probe for each position scanned by a Cartesian robot in the symmetry plane of the plasma jet. Then, by rotating the probe with an angle of $\frac{\pi}{2}$ around its symmetry axis, the mapping of the longitudinal E-field component E_z can be carried out. The interference induced by the probe on the E-field distribution being weak but not null (especially when the probe is in contact with the plasma plume), this experimental configuration with a single probe at the same positions for measuring both radial and longitudinal E-field components minimizes there-

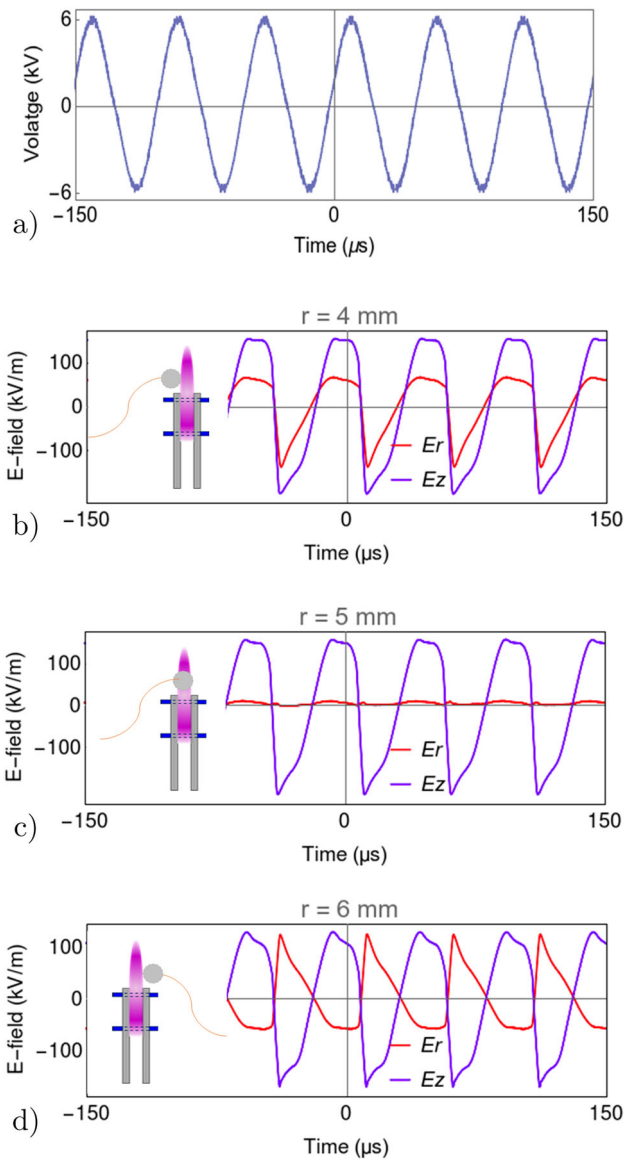

Fig. 5 Temporal evolution of the applied excitation voltage waveform at 18 kHz (**a**) followed by the two orthogonal components of the E-field (E_r and E_z) with the probe. The latter is set at 8.0 mm from the tube outlet in the longitudinal direction. In the radial axis, the origin of the probe is set 4.0 mm from the sidewall of the tube. **b** probe placed on the left side of the tube, **c** within the plasma plume, and **d** on the right side of the tube

fore the potential artifacts. It constitutes the best configuration, especially because the signal to be characterized is reproducible. As an example, the raw temporal traces of E_r and E_z, in presence of the plasma, are given in Fig. 5.

In this measurement set, the transient evolution of the radial component E_r and the longitudinal component E_z are measured with the EO probe placed above the tube outlet. The temporal evolution of the applied voltage is presented in Fig. 5a). The E-field temporal dynamic of the plasma jet is recorded at three characteristic positions: in the top left position of the tube outlet (Fig. 5b), in the middle of the ionization wave propagation (Fig. 5c), and on the top right of the tube (Fig. 5d).

From these graphs, one notices that the EO probe is capable of capturing a periodic signal of both orthogonal components of the E-field having the identical frequency as the high-voltage excitation waveform (i.e. 18 kHz). Qualitatively, it is interesting to compare the E-field magnitude recorded with the EO probe positioned on each side of the plasma plume, i.e., Fig. 5b and d. While the longitudinal component E_z on both sides describe a similar periodic evolution, the signals corresponding to the radial components E_r are reversed. This is explained by the vector characteristic of the E-field induced by the ionization wave propagating in the orthogonal direction. Quantitatively, the magnitude of E_z and E_r are also in remarkable agreement from one side of the APPJ to the other. Focusing on E_z, the longitudinal component field has a slightly stronger amplitude than E_r which is explained by the inherent mechanism of the streamer growth. Indeed, the latter is governed by thin charge space volume formed after the drift of the electrons (having a higher mobility than the ions) leaving the heavy charges quasi-immobile. Ahead of this space charge results an intense E-field oriented along the growth of the streamer. A minor variation of the E_r magnitude is observed between the curves presented in Fig. 5b and d. The reason of this is the absolute position of the EO probe with regard to the axis of the APPJ tube and is directly related to the experimental uncertainties, i.e., ±0.5 mm. This variation of magnitude implicitly reveals the sensitivity of the EO probe to the gradient of the E-field.

Figure 5c corresponds to a situation where the EO probe is right on the guided ionization wave path where a direct interaction between the surface of the sensor is exposed to the discharge. Compared to the previous cases where the EO probe was used in the proper conditions for what it was initially designed, placing the sensor directly in the partially ionized volume is somewhat a controversial experimental scenario. Indeed, the interaction of the probe with the discharge will be discussed more specifically in another section of this paper. Exactingly, the magnitude of the E_r component is reduced at the minimum and tends to 0 kV/m, while the E_z reaches its maximum magnitude. Both observations are fully consistent with each other since a—partially—ionized plasma is electrically neutral at a scale larger than the Debye length. The resulting E-field within this volume is thus hardly above 0 kV/m. From this results, the quasi-absence of radial component of the E-field is observed. However, the E_z component is at its maximum of magnitude peak-to-peak because it corresponds to the E-field of the space charge responsible for the propagation of the ionization wave. In this situation, the E-field is mainly vertical (in the order of 100 kV/m) in contrast to the radial field being almost null. For both components and in all scenario, one will figure that the time evolution of each curve describing the E-field does not entirely resemble the waveform of the

applied voltage (see Fig. 5a). This is again a remarkable signature of the discharge-induced E-field over the Laplacian field. The peculiar features captured by the EO probe on E_z and E_r unveil a rather complex E-field vector profile which will be resolved in the next sections.

2.3 Spatiotemporal evolution of both components of the field

To resolve the spatial and temporal dynamics of the E-field vector, a step-by-step raster scanning with the EO probe is realized in the vicinity of the APPJ device. Practically, both E_r or E_z signals are recorded for several positions above the tube outlet. The step size is set to 0.5 mm, and the origin of the y-axis is set to the tube outlet. This means that the APPJ is pointed upward. A post-treatment is then performed by using Mathematica computational software from Wolfram to reconstruct the E-field vector mapping. This original approach was successfully reported in [63,64] on a pulsed APPJ device, with the pioneered experimental characterization of the vector E-field induced by guided ionization waves.

A sequence of the E-field vector dynamics is presented in Figs. 6, 7 and 8. Each colormap shows the profile of the magnitude of the vector E-field, i.e., $\sqrt{E_z^2 + E_r^2}$. The evolution of the E-field magnitude distribution is revealed with the sequence of colormaps, obtained at different time steps, as shown with the inserts. A quiver plot overlays each color map with white dash lines in order to reveal the E-field lines as well as the direction of the field.

At $t = -2.0$ μs and for an applied voltage lower than 6 kV, one can observe the progressive propagation of the ionization front with the E-field confined along the axis of the tube where flows the helium plume into the ambient air. The streamlines describe an E-field profile pointing downstream, simply because at that moment, the applied voltage just ends its negative half period. It is in the process of rising the voltage potential of the electrode, which is currently higher than the rest of the ionized plasma channel. Note that the surrounding of the plasma plume is at a floating potential. The field is at its maximum in the order of more than 200 kV/m. The axis of the APPJ can be identified where the field is mostly vertical and corresponds to the position $r = 5.0$ mm. Then, the applied voltage increases up to a maximum of 6 kV. At $t = 7.0\,\mu$s, one can observe a distortion of the E-field streamlines in the vicinity of the tube outlet. Intriguingly, one can visibly notice the fall of the field and its total inversion in the two orthogonal directions E_z and E_r. This dynamics of the E-field are in remarkable agreement with the experimental results reported in [63]. Substantial information on the latter work can also be found in [64]. This complex structure of the E-field corresponds to a transition where the applied voltage is passing its maximum amplitude. The electrode transfers its potential to the conductive guided ionization wave channel before to reach a local

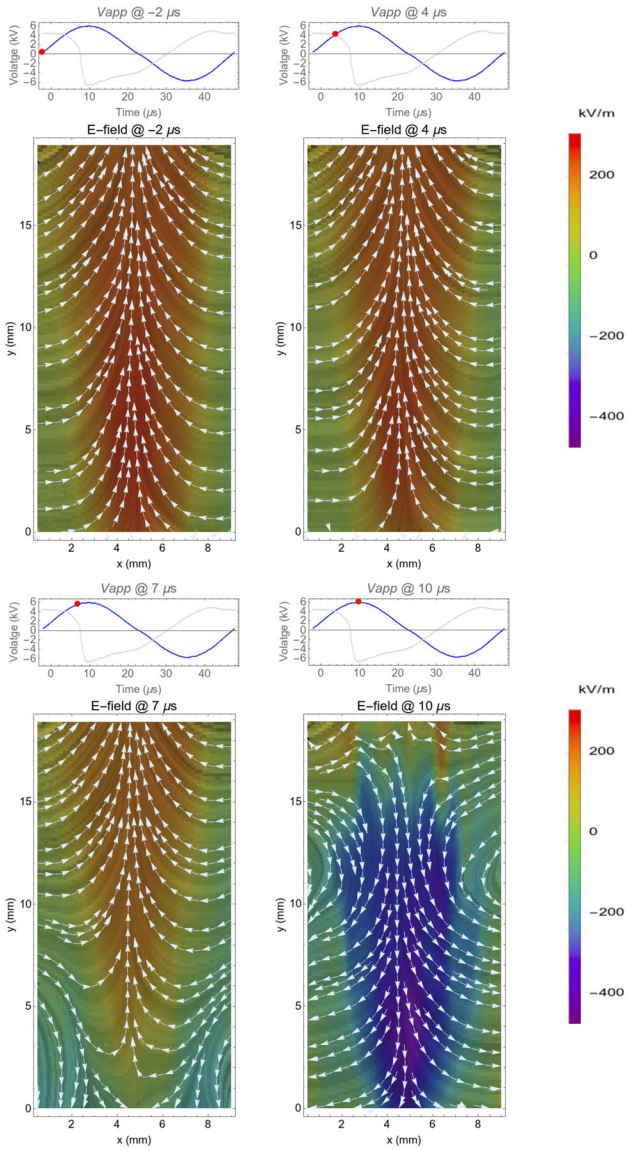

Fig. 6 Spatiotemporal evolution of the E-field vector described by the two orthogonal components E_r and E_z. Top graphics shows the temporal evolution of the applied voltage (blue curve). The color map with the quiver plot depicts the E-field profile in the vicinity of the quartz tube outlet. The red dot indicates the time stamp of the 2D mappings. (continue in Fig. 7)

maximum (blue zone) of about 400 kV/m at $t = 10$ μs. After that, the applied voltage starts to decrease toward zero (at $t = 23$ μs. For this zero voltage, the Laplacian field is zero as well, and we can note that the remaining total field is only induced by the plasma. Beyond this time, the voltage increases again until −6.0 kV (at $t = 35\,\mu$s), and the field reverses once again and increases to reach its maximum (red zone) and so on for the next excitation alternate of the driving applied HV.

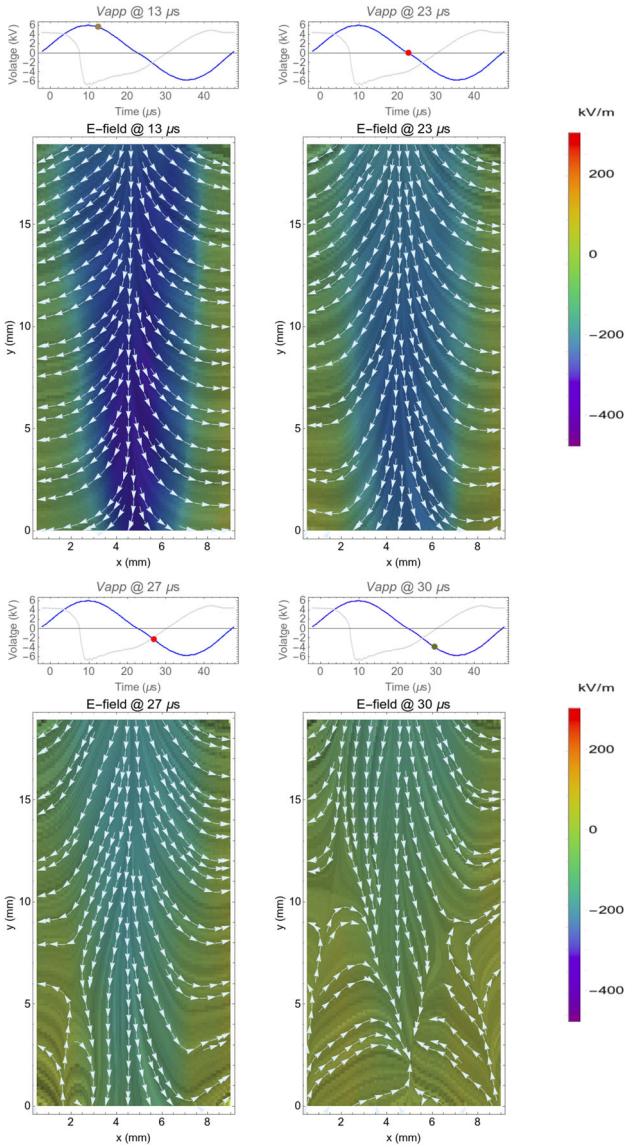

Fig. 7 Following Fig. 6 from $t = 13\ \mu$s to $t = 30\ \mu$s. (continue in Fig. 8)

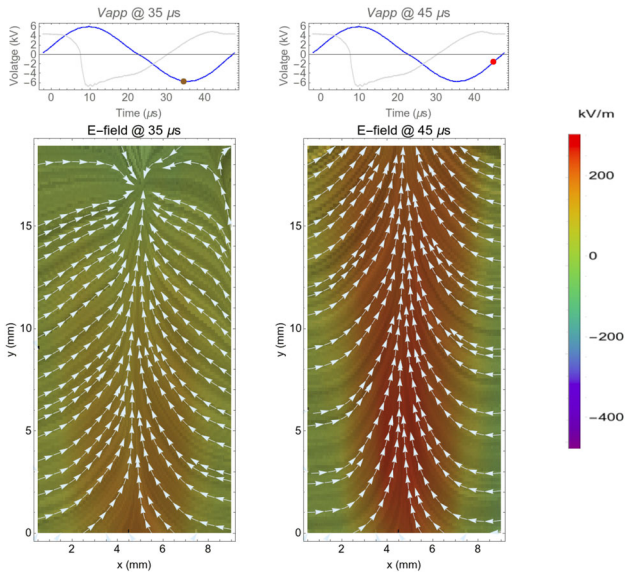

Fig. 8 Following Fig. 7 from $t = 35\ \mu$s and $t = 45\ \mu$s

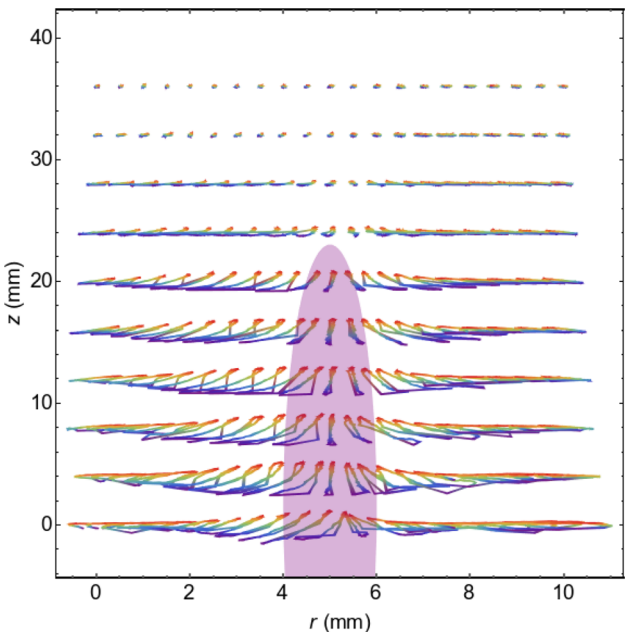

Fig. 9 Polarimetric distribution obtained from a 2D mapping of the two orthogonal field components $\{E_r, E_z\}$ with the exact position of the plasma plume (purple region)

2.4 Polarimetric mapping of the E-field

The temporal evolution of the radial and longitudinal components E_r and E_z of the E-field in the vicinity of the discharge are measured for different positions of the probe. Thanks to high frequency response and the recorded temporal waveforms of each component, a real-time polarimetric analysis can therefore be performed. This representation has the advantage to show a static image of the dynamic evolution of the E-field vector and the phase shift between its two orthogonal components. The synchronized acquisition of the radial and longitudinal components, (E_r and E_z as shown in Fig. 9), gives access to the complete feature of the E-field vector and its temporal evolution. Thus, it offers the possibility to analyze the E-field polarization state spatial distribution. In Fig. 9, the measurements have been performed every 1.0 mm from 0.0 mm to 10.0 mm along the r-axis and at different heights, and every 4.0 mm, and from 0.0 mm to 40.0 mm along the z-axis.

Considering the geometry of the plasma jet, and regarding the previous results, this graph can be divided into two symmetrical parts centered at $r = 5.0\,mm$ (corresponding position of the center of the jet within ± 1 mm uncertainty, as shown in the purple region of Fig. 9). A parametric plot of E_z as a function of E_r allows getting the polarimetric behavior of the field, for different positions of the EO sensor. One can notice

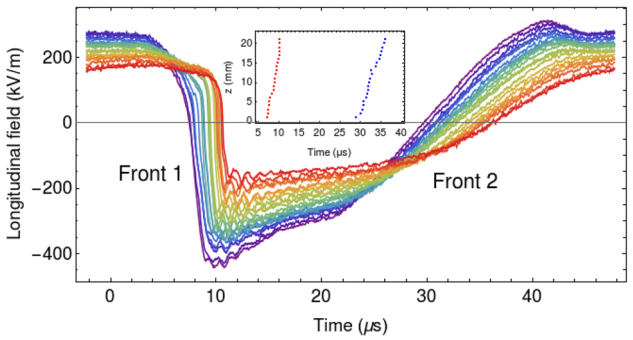

Fig. 10 Temporal evolution of several consecutive acquisitions of the longitudinal component E_z of the E-field corresponding to different vertical position. The inset shows the distance vs time of the front 1 and the front 2 in red and blue, respectively, from which the front velocity is deduced

in Fig. 9 that the field exhibits a linear polarimetric behavior in two specific horizontal locations: (1) along the axis of the plasma jet device where the field remains vertical and corresponds to the direction of propagation of the guided ionization waves and (2) quite far from the symmetry axis where the field becomes horizontal. In all other locations where the field magnitude is significant, a phase shift between E_z and E_r can be observed. The latter describes the E-field profile in the surrounding of the propagation path. It can be considered as a unique signature of the propagated guided streamer.

2.5 Determination of ionization wave front velocity

The E-field being one of the main elementary process responsible for the propagation of the ionization wave front, measuring this quantity is thus also a direct investigation of the streamer growth. In general, the ionization front velocity is experimentally evaluated though the intense emission of light resulting from the direct excitation by electron impact, where the E-field is relatively strong compared to the trail. Commonly, one uses an intensified charge-coupled device (ICCD) camera to capture images of the discharge with short exposure time—typically < 20 ns—to capture the position of the ionization wave front. Then, the growth velocity is inferred from the subsequent images [72–74].

In the present case, to determine the ionization wave front velocity (IWFV), an original method is proposed with a direct measurement of the E-field ahead of the streamer growth. For that purpose, a vertical translation of the EO probe is operated with fine steps in order to record the dynamics of the E-field along the jet. Figure 10 shows several recording of the longitudinal component E_z signal for different vertical position.

One notices on each E_z curve a steep gradient happening at about $(10 \pm 2)\mu$s and corresponds to the front of the ionization wave. A second front with an easier slope can be identified approximately $28\,\mu$s after the first one. It corresponds to the second half period of the high-voltage excitation, where a negative ionization wave is ignited. From the time position of each front, one is able to track the position of the front, as shown in the inset of Fig. 10. The time different from the successive recorded signal allows determining the IWFV directly from the E-field signal. The results reveal a proportional relationship between space and time, meaning a constant propagation velocity for the investigated range. The resulting slope of —z/t— of front 1 corresponds to the IWFV of the positive half period of the excited voltage. An IWFV of 1×10^6 cm/s is found, which is fully consistent with the values reported in the literature [27,74]. Furthermore, a detailed mapping was also done for the radial component E_r around the jet was leading to the same velocity.

3 Perturbation of the field induced by the EO probe

Probe diagnostics used in low-temperature plasmas are inherently considered as intrusive techniques. This is particularly true when part of the probe is directly in contact with the discharge. Thus, the complexity of the plasma surface interactions makes the interpretation of the signals delivered by the sensor challenging and often requires the validation of crucial assumptions. It can also be necessary to partly take into account some elementary mechanisms to be able to extract the desired plasma parameters from the recorded signal. Apart from the plasma surface interaction, probes can also influence the discharge while being in its vicinity. This depends on the type of probe and the nature of the parameter to sense. In the case of E-field, the role of the EO probe may be questioned, and this section aims at giving some piece of answer based on a pragmatic approach.

Practically, to evaluate the intrusive role of the EO probe while sensing vicinity of the APPJ and its generated guided ionization waves, a simple protocol is proposed. One suggests using a set of two identical EO probes, both calibrated with the method previously described. The main idea is then to record several signals with one probe or the other while changing their position in space with regard to the guided streamer propagation. A direct comparison of the recorded waveforms from each probe is then analyzed and discussed. In the next cases, the two probes are set one on top of the other, having their respective orthogonal sensing axis rigorously aligned with each other. The APPJ is set vertically, pointing upward with respect to the gravity force. One of the probe is set about 10 mm toward the APPJ outlet, directly on the propagation path of the guided streamer. Consequently, the latter ends its propagation with a direct interaction with the surface of the probe housing. The second EO probe is positioned strictly above the previously mentioned sensor, and it obviously not in contact with the discharge itself.

In the first case, the EO probe in contact with the guided streamer is considered as a disturbing element

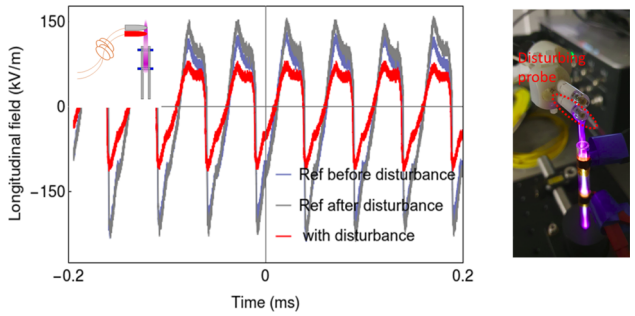

Fig. 11 Temporal evolution of the longitudinal component of the E-field. On the left top corner, the inset describes the relative position of the two probes with regard to APPJ. In this case, the disturbing probe is in red color. On the right-hand side, a photograph depicts the experimental setup with the disturbing probe encircled with a red dash line

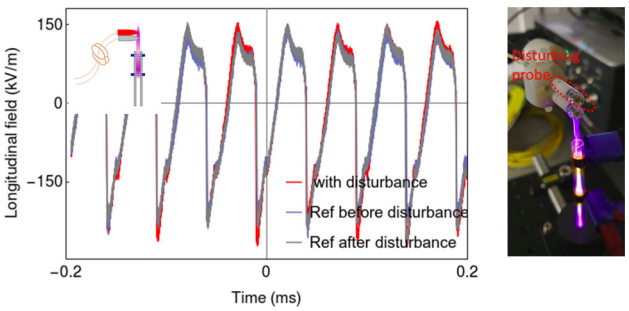

Fig. 12 Temporal evolution of the longitudinal component of the E-field (as shown in Fig. 11). On the left top corner, the inset describes the relative position of the two probes with regard to APPJ. In this case, the disturbing probe is in red color, and thus located *after* the measuring probe. On the right-hand side, a photograph depicts the experimental setup with the disturbing probe encircled with a red dash line

for the E-field measurement which is performed by the upper EO probe.

Figure 11 shows the recorded waveforms with and without the presence of the disturbing probe, as well as a photograph depicting the two EO probes with regard to the APPJ. The goal of this dedicated setup is to evaluate how an EO probe placed between the discharge and the measuring sensor will affect the characterization of the E-field induced by the guided streamer. At the first glance, all signals presented in Fig. 11 are qualitatively comparable. The period and phase are very similar if not identical considering the comparison of the two signals recorded before and after the presence of the disturbing EO probe. This verifies that the probes are well-calibrated, and they measure the same E-field evolution in time. The reproducibility of the measurement is to be notice here.

Concerning the recorded signal in presence of the disturbing EO probe (red curve in Fig. 11), one can figure that neither the period nor the phase or waveform have been affected. Only the magnitude of the signal is reduced compared to the measurements without the disturbing probe. This means that the EO probe inserted between the APPJ and the measuring EO probe is acting as a E-field magnitude attenuator. Indeed, in this configuration, the disturbing probe increases the distance between the charges inducing the plasma-associated field and the measuring probe, thus leading to a decrease in the field magnitude (about 50%). The absence of other discrepancy between the signal with and without disturbance suggests that the inserted EO probe does not have a significant influence on the E-field profile measured downstream, in its vicinity—and within the sensitivity of the sensor.

In the second case, the role of each EO probe is reversed compared to the previous conditions. This means that the EO probe acting as a disturbing element is now placed after the measuring sensor. Figure 12 presents the recorded E-field signals as well as insets for sake of clarity. If the disturbing probe (in red) is not interposed between the measuring probe and plasma, as indicated in the inset of Fig. 12, its impact is expected to be moderate, although this may depend on the type of material.

A metallic antenna would certainly induce some significant modification of the E-field lines, while the case of fully dielectric probes (like the EO probe) should be investigated and discussed. The recorded signals shown in Fig. 12 are remarkably consistent with each other. It is important to mention that the measuring sensor is actually in contact with the guided streamer. Although one cannot really ignore the interaction of the discharge with the EO probe surface of the housing, this interplay does not seem to induce any disturbance on the recorded signal. Not to say that the plasma surface interplay not taking place in this condition, but that it does not have an influence on the measurement within the sensitivity of the probe. As the result, the EO probe diagnostic offers a reasonable possibility to characterize the E-field in guided ionization waves. Some limitation of this technique concerns the properties of the E-field in the vicinity of the plasma surface interface, where the EO probe is not able to sense due to its dimension with regard to the typical plasma sheath thickness at atmospheric pressure (in the order of 10 μm).

4 Conclusion

With this study, the authors demonstrated the remarkable capability of an EO probe to characterize—simultaneously—the temporal and spatial evolution of two orthogonal components of the E-field induced by a guided streamer. This transient discharge—also known as guided ionization wave—was produced by the mean of an APPJ device operated in Helium gas at atmospheric pressure. Prior to the E-field investigation of the discharge, the calibration procedure of the EO probe was performed, considering the peculiarities of the geometry of the APPJ. The temporal and the magnitude sensitivity of the EO probe was compared with

simulations of the E-field without discharge, showing a remarkable sensitivity compare to other methods. The experimental results are fully consistent with the simulation of an electrostatic field taking into account the geometry of the electrodes.

The other aspect of this work deals with the temporal evolution, the polarimetric features and the E-field vector signature of the guided streamer. This EO technique has demonstrated the capability to investigate many temporal features of the E-field profile in space with respect to the sensing EO crystal dimensions. Indeed, the time evolution of the E-field profile could be characterized, evidencing the strong dynamics of the ionization waves and the rather complex structure of the E-field streamlines which mostly drive the electron kinetics of the discharge. The results are fully consistent with previous published work [63,64], especially the dynamic of the field featuring a reversal of the longitudinal component. It has also been possible to measure the growth velocity of the guided streamer by measuring the intense E-field ahead of the ionization column. The values reported in this work are in excellent agreement with theoretical, numerical and experimental studies found in the literature. Finally, a practical approach was proposed to evaluate the potential disturbance of the EO probe on the measurement of the E-field. It has been shown that the impact of the measurement mainly concerns the ability of the electro-optic sensor to measure the absolute magnitude of the E-field. No sign of influence could be found on the phase nor on the time evolution within the sensitivity of the EO probe. The results of this study open new insight on the probe-based diagnostic approach in atmospheric pressure plasmas and their numerous environmental, biological and industrial applications. This method should also be considered in the interaction plasma surfaces, including liquids which will be investigated in the future. Finally, properties of this EO technique can be of major interest for numerous other configurations of plasma experiment such as in vacuum (10^{-5} mbar), even up to microwave frequencies (several tens of GHz).

Author contributions

G.G. led the project. F.A., S.I., M.B., G.C.-G. and L.D. put forward the idea of the research and conceived the experiments. F.A., G.G. and M.B. conducted the experiments. All authors analyzed and discussed the data and results. F.A., G.G. and S.I. wrote the draft manuscript. All authors reviewed the manuscript. All authors have read and agreed to the published version of the manuscript.

Data Availability Statement This manuscript has no associated data or the data will not be deposited. Authors' comment: The data that support the findings of this study are available within the article. Additional data that support the findings of this study are available from the corresponding author upon request.

Declarations

Conflict of interest The authors declare no conflicts of interest.

References

1. G. Colonna, C.D. Pintassilgo, F. Pegoraro, A. Cristofolini, A. Popoli, G. Neretti, A. Gicquel, O. Duigou, T. Bieber, K. Hassouni, L. Laguardia, Theoretical and experimental aspects of non-equilibrium plasmas in different regimes: fundamentals and selected applications. Eur. Phys. J. D **75**(6), 1–35 (2021)
2. D.B. Graves, Low temperature plasma biomedicine: a tutorial review. Phys. Plasmas **21**(8), 080901 (2014)
3. T. Von Woedtke, S. Reuter, K. Masur, K.-D. Weltmann, Plasmas for medicine. Phys. Rep. **530**(4), 291–320 (2013)
4. M. Laroussi, X. Lu, M. Keidar, Perspective: the physics, diagnostics, and applications of atmospheric pressure low temperature plasma sources used in plasma medicine. J. Appl. Phys. **122**(2), 020901 (2017)
5. J. Shen, C. Cheng, S. Fang, H. Xie, Y. Lan, G. Ni, Y. Meng, J. Luo, X. Wang, Sterilization of bacillus subtilis spores using an atmospheric plasma jet with argon and oxygen mixture gas. Appl. Phys. Express **5**(3), 036201 (2012)
6. J.-P. Lim, H.S. Uhm, S.-Z. Li, Influence of oxygen in atmospheric-pressure argon plasma jet on sterilization of bacillus atrophaeous spores. Phys. Plasmas **14**(9), 093504 (2007)
7. K. Lotfy, The impact of the carrier gas composition of non-thermal atmospheric pressure plasma jet for bacteria sterilization. AIP Adv. **10**(1), 015303 (2020)
8. M. Laroussi. Low temperature plasma jets: characterization and biomedical applications, (2020)
9. P.J. Bruggeman, M.J. Kushner, B.R. Locke, J.G.E. Gardeniers, W.G. Graham, D.B. Graves, R.C.H.M. Hofman-Caris, D. Maric, J.P. Reid, E. Ceriani et al., Plasma-liquid interactions: a review and roadmap. Plasma Sources Sci. Technol. **25**(5), 053002 (2016)
10. C. Pattyn, N. Maira, A. Remy, N.C. Roy, S. Iséni, D. Petitjean, F. Reniers, Potential of n 2/o 2 atmospheric pressure needle-water dc microplasmas for nitrogen fixation: nitrite-free synthesis of nitrates. Phys. Chem. Chem. Phys. **22**(42), 24801–24812 (2020)
11. V.V. Kovačević, G.B. Sretenović, B.M. Obradović, M.M. Kuraica, Low-temperature plasmas in contact with liquids-a review of recent progress and challenges. J. Phys. D: Appl. Phys. **55**(47), 473002 (2022)
12. L. Sivachandiran, A. Khacef, Enhanced seed germination and plant growth by atmospheric pressure cold air plasma: combined effect of seed and water treatment. RSC Adv. **7**(4), 1822–1832 (2017)
13. P. Attri, K. Ishikawa, T. Okumura, K. Koga, M. Shiratani, Plasma agriculture from laboratory to farm: a review. Processes **8**(8), 1002 (2020)
14. U.G. Mihiri Ekanayake, D.H. Seo, K. Faershteyn, A.P. O'Mullane, H. Shon, J. MacLeod, D. Golberg, K.K.

Ostrikov, Atmospheric-pressure plasma seawater desalination: Clean energy, agriculture, and resource recovery nexus for a blue planet. Sustain. Mater. Technol. **25**, e00181 (2020)
15. B. Surowsky, O. Schlüter, D. Knorr, Interactions of nonthermal atmospheric pressure plasma with solid and liquid food systems: a review. Food Eng. Rev. **7**(2), 82–108 (2015)
16. H.A.Q. Than, T.H. Pham, D.K.V. Nguyen, T.H. Pham, and A. Khacef. Non-thermal plasma activated water for increasing germination and plant growth of lactuca sativa l. Plasma Chem. Plasma Process., pages 1–17, (2021)
17. E. Moreau, Airflow control by non-thermal plasma actuators. J. Phys. D Appl. Phys. **40**(3), 605 (2007)
18. G.B. Sretenović, P.S. Iskrenović, I.B. Krstić, V.V. Kovačević, B.M. Obradović, M.M. Kuraica, Quantitative analysis of plasma action on gas flow in a he plasma jet. Plasma Sources Sci. Technol. **27**(7), 07LT01 (2018)
19. S. Iséni, C. Pichard, A. Khacef, Monitoring hydrodynamic effects in helium atmospheric pressure plasma jet by resonance broadening emission line. Appl. Phys. Lett. **115**(3), 034102 (2019)
20. A. Bogaerts, T. Xin, J. Christopher Whitehead, G. Centi, L. Lefferts, O. Guaitella, F. Azzolina-Jury, H.-H. Kim, A.B. Murphy, W.F. Schneider et al., The 2020 plasma catalysis roadmap. J. Phys. D: Appl. Phys. **53**(44), 443001 (2020)
21. A. Maroofi, N. Navab Safa, H. Ghomi, Atmospheric air plasma jet for improvement of paint adhesion to aluminium surface in industrial applications. Int. J. Adhesion Adhes. **98**, 102554 (2020)
22. G. Bonizzoni, E. Vassallo, Plasma physics and technology; industrial applications. Vacuum **64**(3–4), 327–336 (2002)
23. T.S.M. Mui, L.L.G. Silva, V. Prysiazhnyi, K.G. Kostov, Polyurethane paint adhesion improvement on aluminium alloy treated by plasma jet and dielectric barrier discharge. J. Adhes. Sci. Technol. **30**(2), 218–229 (2016)
24. C. Pattyn, N. Maira, M. Buddhadasa, E. Vervloessem, S. Iséni, N.C. Roy, M.-P. Antoine Remy, N.D. Delplancke, Geyter, and François Reniers, Disproportionation of nitrogen induced by dc plasma-driven electrolysis in a nitrogen atmosphere. Green Chem. **24**(18), 7100–7112 (2022)
25. S. Hofmann, K. van Gils, S. van der Linden, S. Iseni, P. Bruggeman, Time and spatial resolved optical and electrical characteristics of continuous and time modulated RF plasmas in contact with conductive and dielectric substrates. Eur. Phys. J. D **68**(3), 56–56 (2014)
26. A. Sobota, O. Guaitella, A. Rousseau, The influence of the geometry and electrical characteristics on the formation of the atmospheric pressure plasma jet. Plasma Sources Sci. Technol. **23**(2), 025016 (2014)
27. P. Viegas, E. Slikboer, Z. Bonaventura, O. Guaitella, A. Sobota, and A. Bourdon. Physics of plasma jets and interaction with surfaces: review on modelling and experiments. Plasma Sources Sci. Technol., (2022)
28. Z.-S. Chang, G.-J. Zhang, X.-J. Shao, Z.-H. Zhang, Diagnosis of gas temperature, electron temperature, and electron density in helium atmospheric pressure plasma jet. Phys. Plasmas **19**(7), 073513 (2012)
29. M. Ghasemi, P. Olszewski, J.W. Bradley, J.L. Walsh, Interaction of multiple plasma plumes in an atmospheric pressure plasma jet array. J. Phys. D Appl. Phys. **46**(5), 052001 (2013)
30. C. Douat, G. Bauville, M. Fleury, M. Laroussi, V. Puech, Dynamics of colliding microplasma jets. Plasma Sources Sci. Technol. **21**(3), 034010 (2012)
31. T. Gerling, T. Hoder, R. Brandenburg, R. Bussiahn, K.D. Weltmann, Influence of the capillary on the ignition of the transient spark discharge. J. Phys. D Appl. Phys. **46**(14), 145205 (2013)
32. Q. Xiong, A.Y. Nikiforov, M.A. Gonzalez, C. Leys, L. Xin Pei, Characterization of an atmospheric helium plasma jet by relative and absolute optical emission spectroscopy. Plasma Sources Sci. Technol. **22**(1), 015011 (2012)
33. T. Murakami, K. Niemi, T. Gans, D. O'Connell, W.G. Graham, Chemical kinetics and reactive species in atmospheric pressure helium-oxygen plasmas with humid-air impurities. Plasma Sources Sci. Technol. **22**(1), 015003 (2012)
34. M.E. Pinchuk, G.B. Sretenović, N. Cvetanović, A.A. Dyachenko, B.M. Obradović, O.M. Stepanova, Features of electric field distribution along helium atmospheric plasma jet in stepwise propagation mode of guided streamer. Eur. Phys. J. D **77**(6), 106 (2023)
35. J. Jarrige, M. Laroussi, E. Karakas, Formation and dynamics of plasma bullets in a non-thermal plasma jet: influence of the high-voltage parameters on the plume characteristics. Plasma Sources Sci. Technol. **19**(6), 065005 (2010)
36. V. Samara, Y. Sutton, N. Braithwaite, S. Ptasinska, Acoustic characterization of atmospheric-pressure dielectric barrier discharge plasma jets. Eur. Phys. J. D **74**(8), 169 (2020)
37. J.F. Kolb, A.-A.H. Mohamed, R.O. Price, R. James Swanson, A. Bowman, R.L. Chiavarini, M. Stacey, K.H. Schoenbach, Cold atmospheric pressure air plasma jet for medical applications. Appl. Phys. Lett. **92**(24), 241501 (2008)
38. R.P. Guragain, S. Gautam, D.P. Subedi, R. Shrestha, Effect of plasma treatment on the surface of polyethylene terephthalate with 50hz dielectric barrier discharge at near-atmospheric pressure. Int. J. Recent Res. Rev. **9**(4), 34–37 (2016)
39. V.V. Kovačević, G.B. Sretenović, E. Slikboer, O. Guaitella, A. Sobota, M.M. Kuraica, The effect of liquid target on a nonthermal plasma jet-imaging, electric fields, visualization of gas flow and optical emission spectroscopy. J. Phys. D Appl. Phys. **51**(6), 065202 (2018)
40. G.B. Sretenović, O. Guaitella, A. Sobota, I.B. Krstić, V.V. Kovačević, B.M. Obradović, M.M. Kuraica, Electric field measurement in the dielectric tube of helium atmospheric pressure plasma jet. J. Appl. Phys. **121**(12), 123304 (2017)
41. J.L. Walsh, F. Iza, N.B. Janson, V.J. Law, M.G. Kong, Three distinct modes in a cold atmospheric pressure plasma jet. J. Phys. D Appl. Phys. **43**(7), 075201 (2010)
42. J.-P. Boeuf, L.L. Yang, L.C. Pitchford, Dynamics of a guided streamer ('plasma bullet') in a helium jet in air at atmospheric pressure. J. Phys. D Appl. Phys. **46**(1), 015201–015201 (2013)

43. S. Iseni, A. Schmidt-Bleker, J. Winter, K.-D. Weltmann, S. Reuter, Atmospheric pressure streamer follows the turbulent argon air boundary in a MHz argon plasma jet investigated by OH-tracer PLIF spectroscopy. J. Phys. D Appl. Phys. **47**(15), 152001–152001 (2014)
44. S. Iseni, S. Reuter, A. Schmidt-Bleker, K.-D. Weltmann, Flow and discharge development in an argon atmospheric pressure plasma jet observed by iccd and plif imaging. IEEE Trans. Plasma Sci. **42**(10), 2458–2459 (2014)
45. A.K. Shrestha, R. Shrestha, H.B. Baniya, R.B. Tyata, D.P. Subedi, C.S. Wong, Influence of discharge voltage and pressure on the plasma parameters in a low pressure dc glow discharge. Relation **2**, 122 (2014)
46. M.S. Mann, R. Tiede, K. Gavenis, G. Daeschlein, R. Bussiahn, K.-D. Weltmann, S. Emmert, T. von Woedtke, R. Ahmed, Introduction to DIN-specification 91315 based on the characterization of the plasma jet kINPen MED. Clin. Plasma Med. **4**(2), 35–45 (2016)
47. H. Cheng, X. JiaXing, X. Li, D.W. Liu, L. XinPei, On the dose of plasma medicine: equivalent total oxidation potential (ETOP). Phys. Plasmas **27**(6), 063514 (2020)
48. R. Rutkowski, G. Daeschlein, T. von Woedtke, R. Smeets, M. Gosau, H.-R. Metelmann, Long-term risk assessment for medical application of cold atmospheric pressure plasma. Diagnostics **10**(4), 210 (2020)
49. G.B. Sretenović, I.B. Krstić, V.V. Kovačević, B.M. Obradović, M.M. Kuraica, Spatio-temporally resolved electric field measurements in helium plasma jet. J. Phys. D: Appl. Phys. **47**(10), 102001 (2014)
50. E. Slikboer, A. Sobota, E. Garcia-Caurel, O. Guaitella, In-situ monitoring of an organic sample with electric field determination during cold plasma jet exposure. Sci. Rep. **10**(1), 13580 (2020)
51. E. Slikboer, E. Garcia-Caurel, O. Guaitella, A. Sobota, Charge transfer to a dielectric target by guided ionization waves using electric field measurements. Plasma Sources Sci. Technol. **26**(3), 035002–035002 (2017)
52. Hom Bahadur Baniya, Rajesh Prakash Guragain, Binod Baniya, and Deepak Prasad Subedi. Cold atmospheric pressure plasma jet for the improvement of wettability of polypropylene. Int. J. Polym. Sci., (2020)
53. O. Stepanova, M. Pinchuk, A. Astafiev, Z. Chen, A streamer behavior evolution during an applied voltage cycle in helium and argon atmospheric pressure plasma jets fed by DBD. Jpn. J. Appl. Phys. **59**(SH), SHHC03-16 (2020)
54. M.E. Pinchuk, O.M. Stepanova, M. Gromov, Ch. Leys, A. Nikiforov, Variation in guided streamer propagation along a DBD plasma jet by tailoring the applied voltage waveform. Appl. Phys. Lett. **116**(16), 164102 (2020)
55. N.Y. Babaeva, G.V. Naidis, V.A. Panov, R. Wang, S. Zhang, C. Zhang, T. Shao, Plasma bullet propagation and reflection from metallic and dielectric targets. Plasma Sources Sci. Technol. **28**(9), 095006 (2019)
56. Yuri Petrovich Raĭzer, *Gas Discharge Physics* (Springer, Berlin; New York, 1997)
57. A. Alexander, *Fridman* (Plasma Chemistry. Cambridge University Press, Cambridge, 2012)
58. Yuri Petrovich Raizer, *Gas Discharge Physics* (Springer-Verlag, Berlin, Heidelberg, New-York, 1991)
59. A. Sobota, O. Guaitella, E. Garcia-Caurel, Experimentally obtained values of electric field of an atmospheric pressure plasma jet impinging on a dielectric surface. J. Phys. D Appl. Phys. **46**(37), 372001 (2013)
60. F. Aljammal, G. Gaborit, M. Bernier, S. Iséni, L. Galtier, G. Revillod, L. Duvillaret, Pigtailed electrooptic sensor for time-and space-resolved dielectric barrier discharges analysis. IEEE Trans. Instrum. Meas. **70**, 1–9 (2021)
61. E. Slikboer, O. Guaitella, A. Sobota, Time-resolved electric field measurements during and after the initialization of a khz plasma jet-from streamers to guided streamers. Plasma Sources Sci. Technol. **25**(3), 03LT04 (2016)
62. X. Li, Y. Liu, L. Wang, F. Liu, Z. Fang, Uniformity improvement of plumes in an atmospheric pressure argon plasma jet array by electric field optimization. Eur. Phys. J. D **73**(8), 174 (2019)
63. S. Iséni, Mapping the electric field vector of guided ionization waves at atmospheric pressure. Plasma Res. Express **2**(2), 025014 (2020)
64. S. Iséni, Reply to 'commentary on mapping the electric field vector of guided ionization waves at atmospheric pressure, (2020) plasma res express 2. 025014)'. Plasma Res. Express **4**(1), 018001 (2022)
65. M. Jinno, Y. Ikeda, H. Motomura, Y. Kido, S. Satoh, Investigation of plasma induced electrical and chemical factors and their contribution processes to plasma gene transfection. Arch. Biochem. Biophys. **605**, 59–66 (2016)
66. S.A. Norberg, E. Johnsen, M.J. Kushner, Helium atmospheric pressure plasma jets interacting with wet cells: delivery of electric fields. J. Phys. D: Appl. Phys. **49**(18), 185201 (2016)
67. C.M. Wolff, A. Steuer, I. Stoffels, T. von Woedtke, K.-D. Weltmann, S. Bekeschus, J.F. Kolb, Combination of cold plasma and pulsed electric fields–a rationale for cancer patients in palliative care. Clin. Plasma Med. **16**, 100096 (2019)
68. L. Xinpei, M. Laroussi, V. Puech, On atmospheric-pressure non-equilibrium plasma jets and plasma bullets. Plasma Sources Sci. Technol. **21**(3), 034005 (2012)
69. G. Gaborit, J. Dahdah, F. Lecoche, P. Jarrige, Y. Gaeremynck, E. Duraz, L. Duvillaret, A nonperturbative electrooptic sensor for in situ electric discharge characterization. IEEE Trans. Plasma Sci. **41**(10), 2851–2857 (2013)
70. G. Gaborit, P. Jarrige, Y. Gaeremynck, A. Warzecha, M. Bernier, J.-L. Lasserre, and L. Duvillaret. Pockels' effect-based probe for uwb and hpem measurements. In Frank Sabath and Eric L. Mokole, editors, *Ultra-Wideband, Short-Pulse Electromagnetics 10*, pages 411–421, New York, NY, 2014. Springer New York
71. G. Gaborit, P. Jarrige, F. Lecoche, J. Dahdah, E. Duraz, C. Volat, L. Duvillaret, Single shot and vectorial characterization of intense electric field in various environments with pigtailed electrooptic probe. IEEE Trans. Plasma Sci. **42**(5), 1265–1273 (2014)
72. R. Wang, X. Hui, Y. Zhao, W. Zhu, C. Zhang, T. Shao, Spatial-temporal evolution of a radial plasma jet array and its interaction with material. Plasma Chem. Plasma Process. **39**(1), 187–203 (2019)

73. L. XinPei, M. Laroussi, Dynamics of an atmospheric pressure plasma plume generated by submicrosecond voltage pulses. J. Appl. Phys. **100**(6), 063302 (2006)
74. S. Iséni, A. Baitukha, N. Bonifaci, C. Pichard, A. Khacef, Electrodeless atmospheric secondary induced ionization jet (easii-jet): dynamics and properties of a transferred helium plasma source. Phys. Plasmas **27**(12), 123504 (2020)